

# Rigorous Modeling of Ultrawideband VHF Scattering From Tree Trunks Over Flat and Sloped Terrain

Jiangqi He, Norbert Geng, *Member, IEEE*, Lam Nguyen, and Lawrence Carin, *Fellow, IEEE*

**Abstract**—Three electromagnetic models are employed for the investigation of ultrawideband VHF scattering from tree trunks situated over flat and sloped terrain. Two of the models are numerical, each employing a frequency-domain integral-equation formulation solved via the method of moments (MoM). A body-of-revolution (BoR) MoM formulation is applied for a tree trunk on a flat terrain, implying that the BoR axis is perpendicular to the layers of an arbitrary layered-earth model. For the case of sloped terrain, the BoR model is inapplicable, and therefore the MoM solution is performed via general triangular-patch basis functions. Both MoM models are very accurate but are computationally expensive. Consequently, we also consider a third model, employing approximations based on the closed-form solution for scattering from an infinite dielectric cylinder in free space. The third model is highly efficient computationally and, despite the significant approximations, often yields accurate results relative to data computed via the reference MoM solutions. Data from the three models are considered, and several examples of application to remote sensing are addressed.

## I. INTRODUCTION

SCATTERING from tree trunks plays an important role in many remote sensing applications. For example, in foliage-penetrating (FOPEN) radar, scattering from tree trunks constitutes the principal source of clutter [1]. FOPEN radar systems typically operate at VHF and low-UHF frequencies, for which foliage penetration is reasonably effective. Consequently the canopy-induced clutter [2] is typically much weaker than the clutter signatures induced by dihedral scattering at tree trunks. In particular, several proximate tree trunks can yield composite radar signatures that are very similar to those produced by man-made targets. Before addressing scattering from multiple tree trunks, we must first fully understand the scattered fields induced by a single tree trunk, as a function of terrain topography, this constituting the subject of the present paper.

The scattering of electromagnetic waves via finite-height tree trunks is investigated through development of a method-of-moment (MoM) model for dielectric targets in the presence of a layered medium. Two distinct MoM formulations are considered. In particular, it is often appropriate to model the tree trunk as a

lossy, dielectric body of revolution (BoR), with BoR axis perpendicular to the planar surfaces in the layered medium. Such a MoM model is often termed a 2.5-dimensional (2.5-D) solution, since the basis functions exist along a two-dimensional (2-D) generating arc, with the third dimension accounted for efficiently via cylindrical Fourier harmonics [3]. Consequently, the BoR model is typically computationally much more efficient than a general MoM solution, for which the induced electric and magnetic surface currents on the dielectric surface are expanded in terms of general triangular-patch basis functions [4]. The BoR tree-trunk model is applicable to a general generating arc, and therefore it can be used to investigate the effects of tree curvature on the scattered fields, *vis-à-vis* a simpler model that assumes the tree trunk is a constant-radius cylinder [5].

Despite the attractiveness of the BoR model, it is limited to the case of a flat terrain, i.e., the tree-trunk axis must be perpendicular to the air-ground interface. For the case of a sloped terrain, the BoR model is inappropriate. Consequently, we have developed a separate MoM algorithm, applicable to general dielectric targets embedded in an arbitrary multilayered environment. This MoM model employs the general Rao, Wilton, and Glisson [4] triangular-patch basis functions, and allows the consideration of sloped terrain as well as general tree-trunk shapes.

The two MoM models discussed above are quite powerful for gaining insight into the phenomenology associated with VHF and low-UHF scattering from tree trunks over soil. However, as the target size grows relative to wavelength, they require prohibitive computer memory as well as computation time. Consequently, where possible, it is desirable to use the rigorous MoM models as reference solutions for alternative, approximate models that are computationally efficient. In this context we consider the following approximate model. If we assume that the tree trunk is composed of a constant radius, the electric and magnetic currents on the tree-trunk surface can be approximated by considering scattering from an infinite cylinder in free space, while assuming two incident fields: (1) the direct plane wave, as in free space, plus (2) the contribution due to plane-wave reflection induced by the soil (ground bounce). Moreover, when computing the scattered fields, we must also account for the ground-bounce-induced fields, in a manner similar to that employed for the incident fields. The above model assumes that the surface currents are weakly affected by diffraction induced at the ends of the finite-height tree trunk. Lin and Sarabandi [5] considered a similar model, in which they also accounted for the effects of the tree bark. However, the focus of [5] was on microwave scattering, for which the tree bark is often important. Here we are primarily interested in FOPEN radar, and at the VHF and low-UHF frequencies associated with such, the

Manuscript received December 9, 1999; revised October 25, 2000.

J. He and L. Carin are with the Department of Electrical and Computer Engineering, Duke University, Durham, NC 27708-0291 USA.

N. Geng is with the Institute for Microwaves and Electronics, University of Karlsruhe, Karlsruhe, Germany.

L. Nguyen is with the Army Research Laboratory, AMSRL-SE-RU, Adelphi, MD 20783 USA.

Publisher Item Identifier S 0196-2892(01)08838-6.

tree bark is expected to be of secondary consideration. We note that in [5], the authors did not have access to a numerically rigorous model such as the MoM, and therefore, the accuracy of the aforementioned approximate model could not be confirmed. Our reference MoM solution allows us to perform such a calibration.

The scattering of electromagnetic waves from trees has been investigated by several authors using numerous techniques [6]–[11]. In addition to the aforementioned infinite-cylinder model [5], authors have examined the use of volumetric electric-field integral equations, solved via an electric-dipole model [9]. This algorithm is applicable to tree models far more realistic [9] than a simple finite-length cylinder. In [9], the free-space Green’s function was employed with appropriate reflection coefficients appended to account for soil interactions. Authors have also considered scattering from multiple trees [6], [8], employing, for example, an iterative procedure to account for intertree electromagnetic interaction [6]. In [6], the fields within a given tree (finite-length dielectric cylinder) are computed via an infinite-cylinder model, however the scattered fields from the cylinders are computed using the dyadic half-space Green’s function. In the work employed here, in the context of our MoM solutions, we employ a surface-integral-equation formulation, and the currents on the target surface are computed rigorously through explicit use of the half-space Green’s function (the scattered fields are also computed via the half-space Green’s function).

The remainder of the paper is organized as follows. The details of the two MoM models employed here have been elucidated elsewhere [3], [12], and therefore in Section II, we provide a brief overview of these techniques. Their application to computing the tree-trunk radar cross section (RCS) is provided in some detail, such that it is understood how we account for diffractive effects induced at the top of the (modeled) tree trunk. Finally, we also briefly summarize the approximate model, the details of which are found in [5]. In Section III, a large set of results are presented, in which we examine tree-trunk scattering from several perspectives. In particular, we compare the relative accuracy of the approximate and two MoM solutions, for flat and sloped terrain. Several phenomenological examples are addressed, including the aspect-dependent synthetic aperture radar (SAR) signature of a tree trunk on a sloped terrain.

## II. THEORETICAL FORMULATION

### A. Method-of-Moments (MoM) Analyses

We have developed MoM models applicable to a dielectric body of revolution (BoR) embedded in an arbitrary layered medium, as well as for a general dielectric target also embedded in an arbitrary layered medium [3], [12]. For the former, along the target-generating arc, we employ the subsectional basis functions discussed in [3], while for the latter, we employ the general triangular-patch basis functions introduced in [4]. MoM scattering models for BoR and general dielectric targets have been available for over a decade for the case of the target residing in free space [13]. To consider scattering from such a target embedded in an arbitrary layered medium, the problem

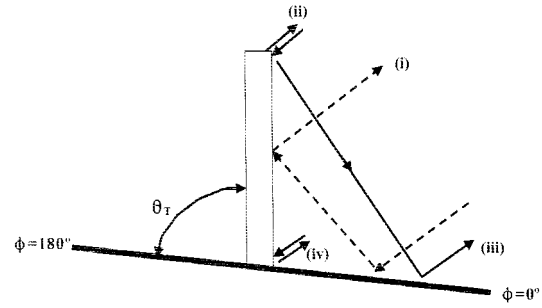


Fig. 1. Schematic of a lossy dielectric cylinder (model tree trunk) on a sloped terrain. Four scattering mechanisms, discussed in the text, are identified.

is complicated significantly by the need to compute the layered-medium dyadic Green’s function [14]. As is well known, in general, each component of the dyadic Green’s function cannot be represented in closed form, but must be expressed in terms of a generally highly oscillatory Sommerfeld integral [14], [15]. The efficient evaluation of such integrals has been the principal bottleneck to generalizing the free-space models in [13] to the case of general layered media.

Recently the method of complex images has been developed, in which a fit is performed to the spectral Green’s function, along a salutary path in the complex spectral space. The fit is performed using a sum of exponentials, each with a complex argument [3], [16], [17]. The attractiveness of this approach is that, once the sum of exponentials is fit to the spectral Green’s function, a closed-form inversion exists for the Sommerfeld integral associated with each exponential, cumulatively yielding the space-domain Green’s function. Here we use a Prony [18] fitting procedure, although any of a number of such techniques are available [19]. The complex-image technique is most effective when the target lies entirely within a single layer, since in this case all source and observation points are also within the same layer. Under this circumstance the spectral fit is performed once, for each dyadic component, for all source and observation points, significantly accelerating computational efficiency. For scattering from tree trunks, the dielectric scatterer is entirely above the soil (we ignore the root system) and therefore the complex-image technique offers an attractive means of implementing both of the aforementioned MoM models. The interested reader is referred to [3], [16], [17] for more details on the complex-image technique.

### B. Scattering Mechanisms

As indicated, the details of the MoM formulations can be found elsewhere [3], [12] and therefore, here we focus on issues of particular interest to tree-trunk scattering. In particular, consider plane-wave scattering from a finite-length tree trunk over soil, as shown in Fig. 1. There are four principal scattering mechanisms: i) a dihedral response due to the tree-soil interaction; ii) direct diffraction from the top of the tree trunk; iii) diffraction from the top of the tree trunk followed by a ground bounce; and iv) diffraction from the bottom of the tree trunk (at the air-ground interface). In addition to these scattering mechanisms, there are multiple interactions between the four, as well as other higher order effects. Scattering mechanisms (ii)–(iv) are

always present in the far-zone *backscattered* fields, while i) is present when the tree trunk is normal to the air-ground interface (e.g., flat terrain) and for special incident angles [5] when the terrain is sloped.

It is important to emphasize that, for a real tree with a branch and leaf structure, the diffraction mechanisms from the “top” of the tree will be different than those in Fig. 1. However, if there is a backscattered dihedral effect observed at the sensor (flat terrain), it is typically much stronger than leaf and branch scattering at VHF frequencies, and therefore mechanism i) dominates. To explore this backscattered effect in detail, when it exists, we perform the following procedure. Considering Fig. 1, scattering mechanism ii) is observed earliest in time, for transient excitation of sufficient resolution (wide enough bandwidth). To investigate the radar cross section (RCS) of mechanism i), we window out in time the contribution from ii), leaving principally the time domain response of i), iii), and iv). Mechanisms iii) and iv) can be viewed as components of i), when the latter is observed in backscatter, with the sum of the two generally being much weaker than mechanism i), which typically occurs during an overlapping time window. After windowing out ii), the transient scattered waveform is converted back to the frequency domain, the incident-pulse spectrum removed (deconvolved), yielding an approximation for the RCS of i). As elucidated above, this model will well represent the backscattered dihedral response at VHF frequencies, when it exists, despite the fact that the leaf and branch structure are ignored.

For the case of sloped terrain, scattering mechanism i) is generally *not* observed in backscatter, leaving mechanisms ii)–iv). Like the dihedral effect i), scattering mechanism iv) is generally weakly affected by the leaf and branch structure. However, mechanisms ii) and iii) are driven primarily by diffraction at the “top” of the tree trunk, this ignoring effects of the leaves and branches. As mechanisms ii)–iv) will generally drive the backscattered signature for the case of sloped terrain, it is important to emphasize that the aforementioned approximations must be confirmed via VHF measurements, this constituting an important area of future research. We note as well that the MoM model with triangular-patch basis functions, discussed above, can in principle be used to model the tree branch structure, with the leaves generally being of secondary importance at VHF frequencies. This too is an area of future work.

### C. Data Format

Below we present both frequency- and time-domain results, with the former presented as RCS. For examples in which the terrain is flat (tree trunk normal to the air-ground interface), the RCS is principally characterized by the dihedral scattering represented by i) in Fig. 1, where we have windowed out the effects of ii) as discussed above. For sloped terrain, mechanism i) is typically not present in backscatter, and therefore the RCS in this case is representative of mechanisms ii)–iv), plus associated higher-order effects. All scattering mechanisms are retained in the time-domain results, such that the associated phenomena are observed. The far-zone time-domain backscattered results are

normalized as follows. The frequency-domain, far-zone polarimetric scattering matrix can be expressed as

$$\begin{bmatrix} E_V^{scat} \\ E_H^{scat} \end{bmatrix} = \frac{\exp(-jk_1 r)}{r} \begin{bmatrix} S_{VV} & S_{VH} \\ S_{HV} & S_{HH} \end{bmatrix} \begin{bmatrix} E_V^{inc} \\ E_H^{inc} \end{bmatrix} \quad (1)$$

where  $k_1$  is the wavenumber of the top region (usually air), and  $r$  is the nominal far-zone distance from the target to the observer. The *normalized* time-domain results are defined as

$$\begin{bmatrix} w_{VV}(t) & w_{VH}(t) \\ w_{HV}(t) & w_{HH}(t) \end{bmatrix} = \frac{1}{2\pi} \int_{-\infty}^{\infty} \begin{bmatrix} S_{VV}(\omega) & S_{VH}(\omega) \\ S_{HV}(\omega) & S_{HH}(\omega) \end{bmatrix} \begin{bmatrix} P_V(\omega) \\ P_H(\omega) \end{bmatrix} \exp(j\omega t) d\omega \quad (2)$$

where  $P_V$  and  $P_H$  represent the frequency dependence of the  $V$  (vertical) and  $H$  (horizontal) polarized incident-field components.

### D. Series Approximation

The MoM yields a rigorous solution for the electric and magnetic surface currents induced on the target surface, from which the scattered fields can be computed. If the tree trunk is assumed to be a constant-radius dielectric target, with possibly multiple concentric layers, one can employ the exact solution for free-space scattering from an infinite dielectric cylinder [5]. The tangential electric and magnetic fields on this infinite target can be used to approximate the electric and magnetic surface currents on a finite-length dielectric cylinder. Moreover, the solution must be modified slightly to account for ground-bounce scattering [5]. For comparison, we consider such an approximate model, for a lossy dielectric cylinder over a flat and sloped half space. Here we assume the cylinder is homogeneous, although it is straightforward to extend the model to account for tree layering [5].

## III. EXAMPLE RESULTS

### A. Comparison Between Two MoM Models

As discussed in Section II, two MoM formulations have been implemented, one assuming that the dielectric target is a body of revolution (BoR) and the other employing general triangular-patch basis functions [4], the latter applicable to general dielectric targets. We begin by comparing the results computed by these two models, for the special case of a BoR tree trunk, and therefore we assume flat terrain. Moreover, although the MoM models are applicable to general layered media, here and throughout the paper we assume the soil is a lossy, dispersive half space. We perform the comparisons in the time domain, assuming time-domain plane-wave excitation with the incident pulse in Fig. 2. This waveform encompasses the VHF and low-UHF frequency bands. The upper frequency considered is dictated by the memory and computation-time (CPU) requirements of the MoM models. In particular, the size of the subsectional basis functions must be small relative to the wavelength in the tree trunk [3], [13], and therefore the number of basis functions  $N$  grows precipitously as the target size increases relative to wavelength i.e., as the frequency

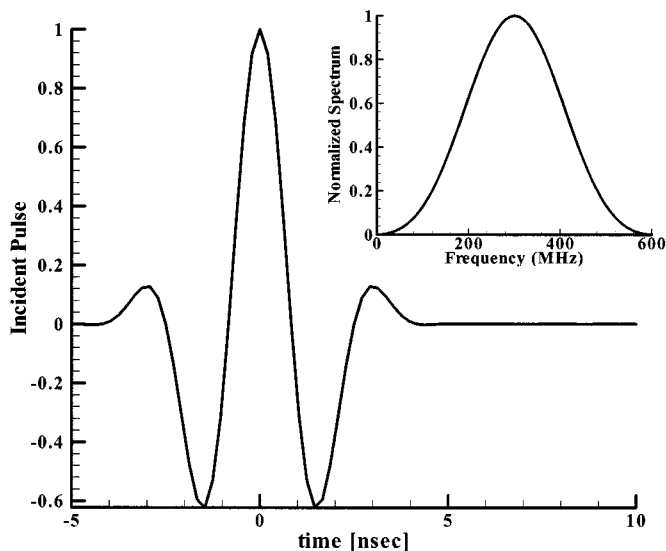


Fig. 2. Incident pulse and associated spectrum, used for the time-domain scattering examples.

increases). For a traditional MoM analysis, the memory requirements are order  $N^2$  and the CPU requirements are order  $N^3$ , for a direct solution of the MoM matrix equation (the CPU is order  $PN^2$  for a conjugate-gradient solver, where  $P$  is the number of conjugate-gradient iterations). We note that the BoR model is typically more efficient from both a memory and CPU perspective than the triangular-patch model, since the basis functions for the former only exist along a 2-D generating arc [3]. However, the number of azimuthal modes [3] required of the BoR model increases with target electrical size, i.e., with increasing frequency), and therefore the BoR model is as well limited in the target size that can be considered.

In Fig. 3, we compare the time-domain scattered fields computed via the two models, considering tree trunks of 30 cm diameter and heights of 3, 4, and 5 m, for an incidence angle of  $50^\circ$  relative to the normal ( $40^\circ$  relative to grazing). The tree trunk is characterized by the complex permittivity  $\epsilon = \epsilon_0(3 - j0.5 - j\sigma/\omega\epsilon_0)$  with conductivity  $\sigma = 0.005$  S/m, where  $\epsilon_0$  is the free-space permittivity. The soil is representative of Yuma soil with 10% water content (see [20]). The  $VV$  and  $HH$  scattered fields are presented in Fig. 3(a) and 3(b), respectively. For this BoR target, the cross-polarized *backscattered* fields are zero [21]. We first note that the agreement between the two MoM solutions is generally good, although there are slight differences near the peaks of the waveforms, these associated with the relatively high-frequency components of the waveform. This is attributed as follows. For the BoR model, we employed a minimum of ten subsectional basis functions per wavelength inside the tree trunk, while for the triangular-patch model, at the highest frequencies (see Fig. 2) we applied approximately six basis functions per wavelength. The latter discretization was applied due to the required three-dimensional (3-D) current expansion on the target surface, this becoming computationally expensive as the frequency increases (see discussion in previous paragraph). Nevertheless, the two solutions are in good agreement.

Focusing now on the phenomenology reflected in Fig. 3, we note that, as expected, the time-domain scattered fields are char-

acterized initially by direct diffraction from the “top” of the tree trunk. The tree height and bandwidth are sufficient that this effect, mechanism ii) in Fig. 1, is resolvable in time from the other scattering effects. As expected, the initial scattered waveform is independent of the tree height. By contrast, the second return, this representing a composite of mechanisms i), iii), and iv) from Fig. 1, grows with increasing tree-trunk height. In fact, this portion of the scattered waveform is almost a linear function of the tree-trunk height. A notable distinction seen in Fig. 3 is that the dihedral response i) in Fig. 1 is significantly larger for the  $HH$  scattered fields relative to the  $VV$  case. This is attributed to generally enhanced penetration at a dielectric interface for vertically polarized incidence relative to the horizontal case, thereby diminishing the dihedral interaction between the soil and the tree trunk. For the soil considered here, the Brewster angle is approximately  $65^\circ$  (the soil is dispersive so the Brewster angle is frequency dependent, and moreover, since the soil is lossy, the concept of a Brewster angle is itself approximate). The  $50^\circ$  angle of incidence at the soil interface therefore yields considerable penetration for V polarization, with this significantly less for H polarization.

Before leaving Fig. 3, we note that for both the  $VV$  and  $HH$  cases, there are relatively little scattered fields after the principal dihedral response. This implies that, for the target considered, there is little multiple interaction between the various scattering mechanisms.

### B. Diameter and Electrical Properties of Tree Trunk

The previous example served to validate the relative accuracy of the two MoM solutions and to provide an introduction to the tree-trunk scattering phenomenology. However, the results in Fig. 3 addressed a single tree diameter and tree trunks of fixed electrical parameters. Addressing the latter, the electrical parameters of tree trunks are expected to be a strong function of the tree type as well as of the season. In the next set of examples, we consider trees composed of the electrical parameters considered in Fig. 3.  $\epsilon = \epsilon_0(3 - j0.5 - j\sigma/\omega\epsilon_0)$  and  $\sigma = 0.005$  S/m as well as tree trunks characterized by  $\epsilon = \epsilon_0(10 - j2 - j\sigma/\omega\epsilon_0)$  and  $\sigma = 0.02$  S/m. An investigation of these relatively disparate examples will help quantify the effect of the tree electrical parameters on the scattered signature. Moreover, the tree height is fixed at 5 m, the terrain is assumed flat, composed of Puerto Rico clay soil [22], and several tree-trunk diameters are considered. Although we consider a fixed tree height in these examples, the data in Fig. 3 indicate that these results will scale linearly with varying tree-trunk height. Finally, as discussed in Section II-B and Section II-C, the frequency-domain RCS calculations presented here do not include scattering mechanism ii) in Fig. 1 (it being windowed out in the time domain).

Having demonstrated the relative accuracy of the two MoM solutions, for the case in which the tree trunk is normal to the air-ground interface, here we only consider computations performed with the BoR MoM model. Further, for comparison, we also consider scattered fields computed via the approximate series-solution-based model [5] discussed in Section II-D. In Fig. 4, we consider the RCS computed by these two models for tree trunks characterized by  $\epsilon = \epsilon_0(3 - j0.5 - j\sigma/\omega\epsilon_0)$  and

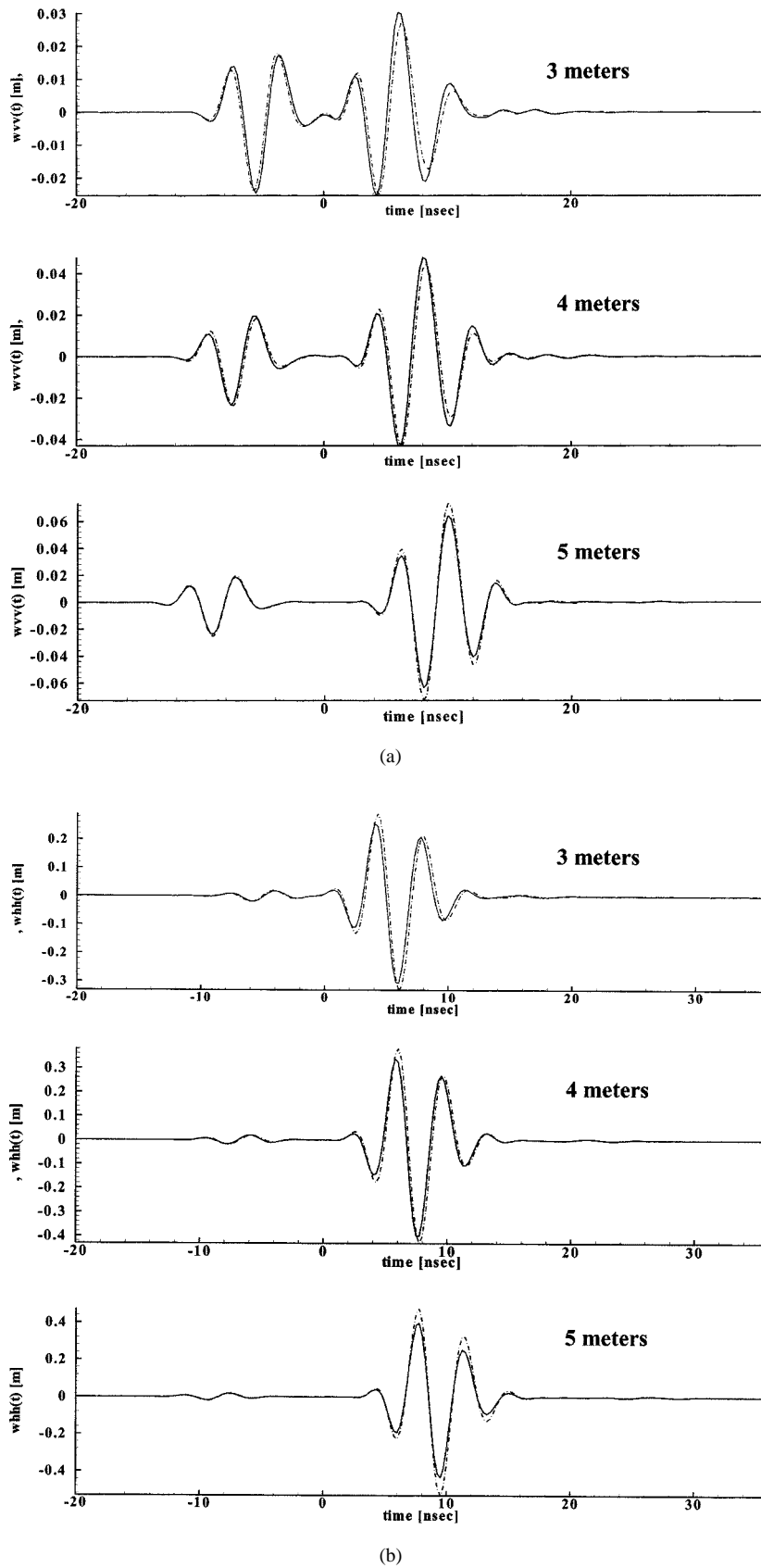
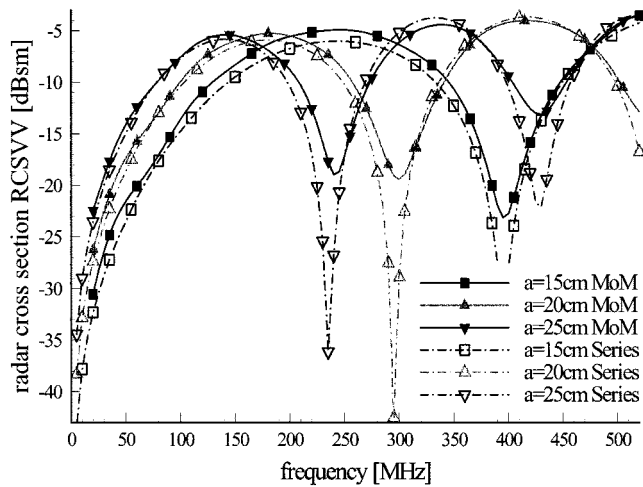
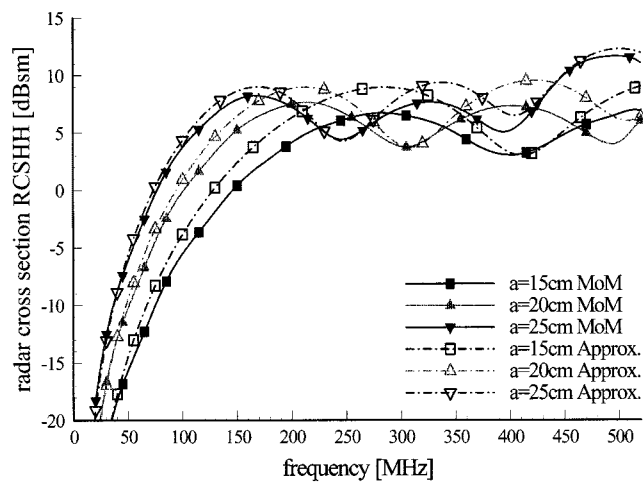


Fig. 3. Time-domain waveform backscattered from a lossy dielectric cylinder (complex permittivity  $\epsilon = \epsilon_0(3 - j0.5 - j\sigma/\omega\epsilon_0)$  with conductivity  $\sigma = 0.005$  S/m) situated atop a half space composed of Yuma soil with 10% water content [20]. The tree trunk has a 30 cm diameter, and is normal to the air-ground interface. The pulsed plane wave has the shape shown in Fig. 2, and is incident at  $50^\circ$  relative to the normal, and results are shown for trunk heights of 3, 4, and 5 m. The solid curves were computed via the body of revolution MoM model [3], and the dashed via the triangular-patch model [12]. (a)  $VV$  polarization and (b)  $HH$  polarization.



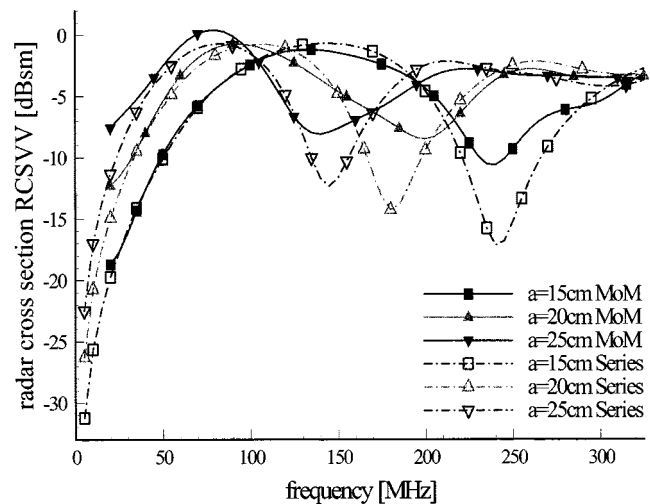
(a)



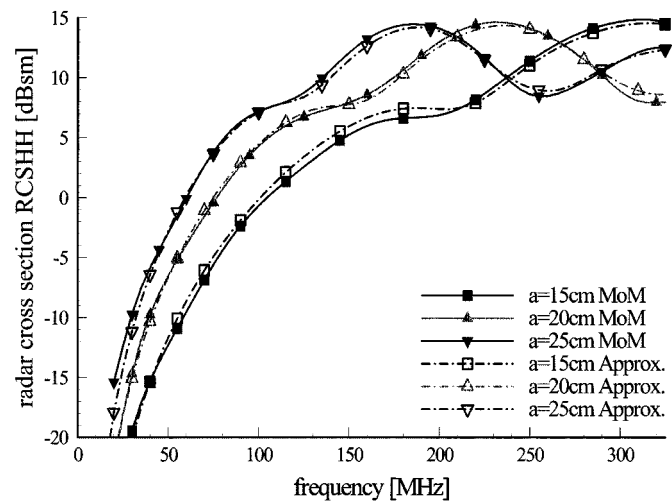
(b)

Fig. 4. Radar cross section (RCS) of a tree trunk normal to a half-space interface, with the half space electrical properties characteristic of Puerto Rico clay [22], and the plane wave is incident at  $60^\circ$  relative to the air-soil normal. The tree trunks are characterized by  $\epsilon = \epsilon_0(3 - j0.5 - j\sigma/\omega\epsilon_0)$  with  $\sigma = 0.005$  S/m, and tree diameters of 30, 40, and 50 cm are considered. The solid curves represent the BoR MoM solution [3], and the dashed curves the approximate series solution [5]. (a)  $VV$  polarization and (b)  $HH$  polarization.

$\sigma = 0.005$  S/m for tree diameters of 30, 40, and 50 cm. The plane-wave incident angle is  $60^\circ$  relative to the air-soil normal. We again note that the  $VV$  response [Fig. 4(a)] is markedly smaller than that for the  $HH$  polarization [Fig. 4(b)]. We also note that, as expected, the RCS increases with frequency as the wavelength becomes smaller relative to the tree-trunk diameter (approaching the “optical” regime). Consequently, the frequency at which the RCS starts to reach its maximum increases as the tree diameter decreases. There are several other interesting scattering mechanisms playing a role in this example. In particular, note that, in the high-frequency region, the RCS is characterized by frequency-dependent dips in the RCS response, with these dips particularly strong for  $VV$  polarization. This phenomenon is also closely related to the tree-trunk diameter since the dips scale to lower frequencies as the diameter increases. We therefore attribute these dips to frequencies at which, in backscatter, the superposition of the fields scattered from the front and back of the tree trunk destructively interfere.



(a)

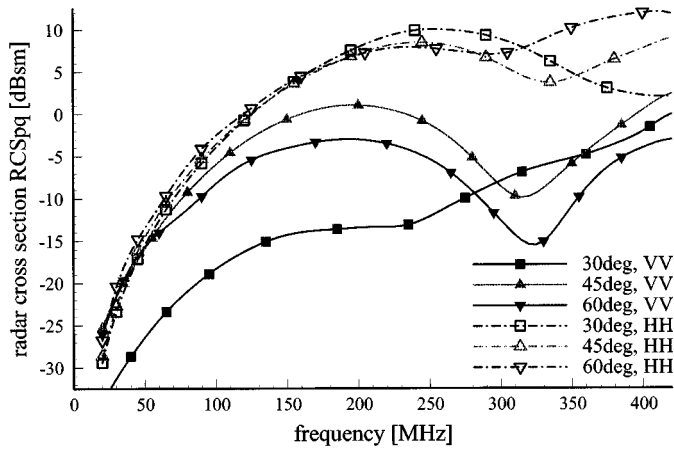


(b)

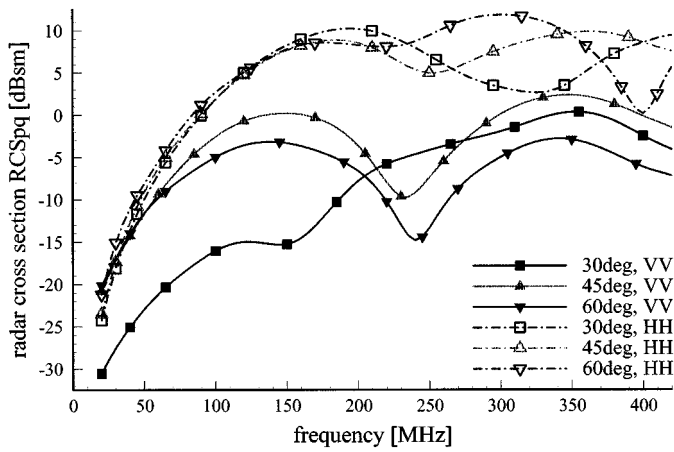
Fig. 5. As in Fig. 4, but now the tree trunks are characterized by  $\epsilon = \epsilon_0(10 - j2 - j\sigma/\omega\epsilon_0)$  with  $\sigma = 0.02$  S/m. (a)  $VV$  polarization and (b)  $HH$  polarization.

This phenomenon is expected to be stronger for  $VV$  polarization, since the penetration into the tree trunk is expected to be larger in this case.

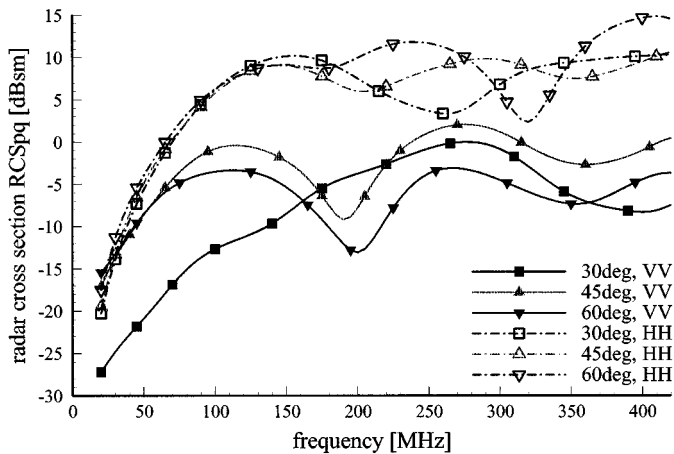
Another matter of note is the relative agreement between the MoM and the approximate series solution [5] for the target RCS. In Fig. 4(a), the agreement between these two models is good for the  $VV$  case, while for the  $HH$  polarization considered in Fig. 4(b) the agreement is excellent, especially for the largest diameter considered. Recall from Fig. 1 that, in addition to the dihedral response characterized by mechanisms i) and iv), there are scattered fields induced by top diffraction followed by a ground bounce, reflected by mechanism iii). For the  $HH$  case, the cumulative effects of i) and iv) are expected to be large, with this less so for  $VV$  polarization (due to enhanced penetration for the latter). Consequently, mechanism iii) is expected to be of stronger *relative* strength for  $VV$  than for  $HH$  polarization. The approximate RCS calculation, based on the series solution for an *infinite* cylinder [5], does not provide a good representation for the diffraction induced at the top of the tree trunk. As noted, this effect is of greater relative importance for the  $VV$



(a)



(b)

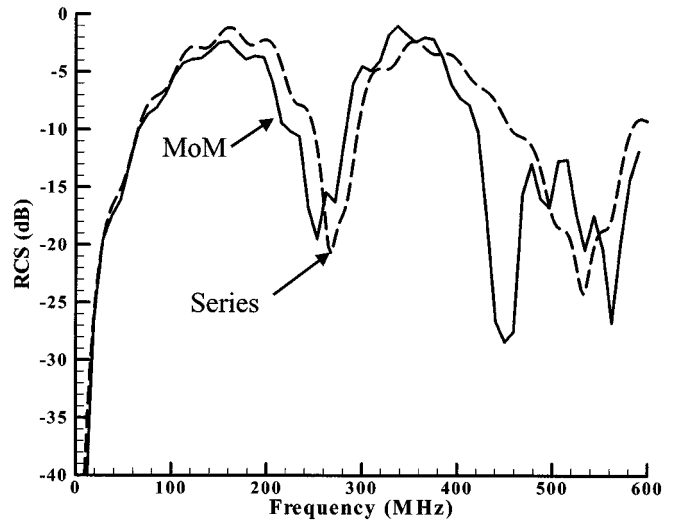


(c)

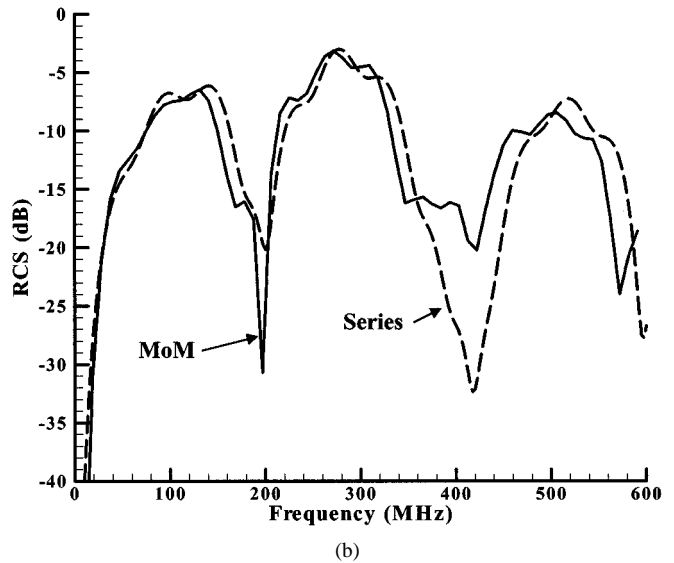
Fig. 6. Radar cross section of tree trunks composed of permittivity  $\epsilon = \epsilon_0(5 - j1 - j\sigma/\omega\epsilon_0)$ , with conductivity  $\sigma = 0.01$  S/m, 5 m trunk height, and the half space is modeled as Puerto Rico clay [22]. The trunks are normal to the air-soil interface, and the plane wave is incident at  $30^\circ$ ,  $45^\circ$ , and  $60^\circ$  relative to the normal to the air-soil interface. (a) 30-cm tree diameter, (b) 40-cm tree diameter, and (c) 50 cm tree diameter.

case, and therefore the approximate series solution is expected to be less accurate for this polarization.

In Fig. 5, we consider the same example as in Fig. 4, but now the permittivity and conductivity of the target are raised to  $\epsilon = \epsilon_0(10 - j2 - j\sigma/\omega\epsilon_0)$  and  $\sigma = 0.02$  S/m. We expect less



(a)



(b)

Fig. 7. Radar cross section for  $HH$  polarization, for a  $10^\circ$  sloped terrain with electrical properties characteristic of Yuma soil with 10% water content [20]. The tree-trunk diameter is 30 cm, its height is 5 m, and its electrical properties are characterized by  $\epsilon = \epsilon_0(3 - j0.5 - j\sigma/\omega\epsilon_0)$  with conductivity  $\sigma = 0.005$  S/m. The azimuthal angle  $\phi = 0^\circ$  corresponds to viewing up the slope, with  $\phi = 180^\circ$  viewing downward (see Fig. 1). The solid line represents the MoM solution [12] and the dashed curve the approximate series-based solution [5], assuming  $50^\circ$  incidence relative to the axis of the tree trunk. (a)  $\phi = 0^\circ$  and (b)  $\phi = 180^\circ$ .

penetration into the tree trunk for this high-contrast case, and therefore, the dips seen in Fig. 4 as a function of frequency are less dramatic for this case. Note also that the frequency at which the RCS becomes relatively constant with frequency is smaller in Fig. 5 than in Fig. 4 due to the enhanced electrical size of the target with increased permittivity. In this context, note that in Fig. 5, the MoM computations were only performed up to 325 MHz, while those in Fig. 4 were performed up to 520 MHz. This again is reflective of the target electric size, and the associated enhanced computational requirements (see Section IIIA) as the target permittivity increases. It is interesting to also note that, for the higher permittivity in Fig. 5, the agreement between the approximate and MoM-computed RCS is very good for  $HH$  polarization, while being slightly less good for  $VV$ .

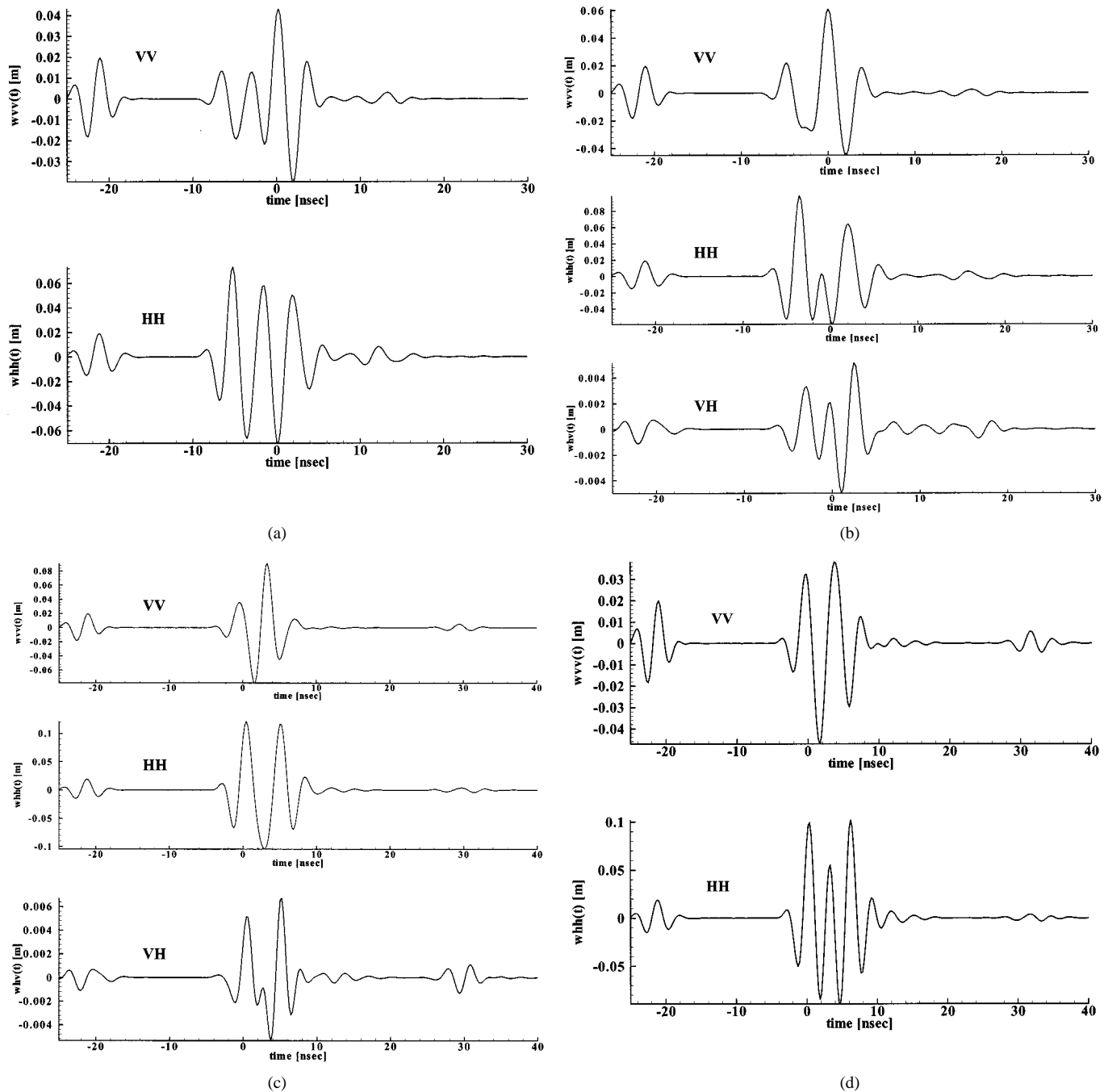


Fig. 8. Time-domain backscattered fields from the tree trunk considered in Fig. 7, assuming an incident pulse as shown in Fig. 2. The pulsed plane wave is incident  $50^\circ$  from the axis of the tree trunk. (a)  $\phi = 0^\circ$ , (b)  $\phi = 45^\circ$ , (c)  $\phi = 135^\circ$ , and (d)  $\phi = 180^\circ$ .

### C. Angle of Incidence

In the previous set of examples, the angle of incidence was held constant while other parameters were varied. When performing synthetic aperture radar (SAR) measurements, the angle between the tree trunk and sensor is dictated, for a fixed sensor height, by the distance between the sensor and scatterer. Consequently, two identical tree trunks at different portions of the SAR image will be interrogated with distinct angles of incidence. We therefore examine the effect of the incidence angle on the RCS of a tree trunk on flat terrain, assuming the same soil type as in Figs. 3–5. We consider tree trunks composed of permittivity  $\epsilon = \epsilon_0(5 - j1 - j\sigma/\omega\epsilon_0)$  and conductivity  $\sigma = 0.01$  S/m, with 5 m height. In Fig. 6(a)–(c), we plot the computed RCS for tree diameters of 30, 40, and 50 cm.

The frequency-dependent soil parameters are again characterized as Puerto Rico clay [22]. As expected, the increasing tree-trunk diameter (with all other parameters fixed) principally results in a shifting of the RCS characteristics to lower frequencies. As we have found throughout, at frequencies greater than approximately 30 MHz, the  $HH$  RCS is consistently stronger than its  $VV$  counterpart.

From Fig. 6, we note that the angle of incidence has an important effect on the tree-trunk RCS, with this particularly true for  $VV$  polarization. In fact, at low frequencies the  $HH$  RCS is almost independent of incidence angle, with a larger variation occurring with increased frequency. This is to be expected, since for  $VV$  polarization there is relatively strong penetration into the tree trunk, and the scattering induced by the transmitted compo-

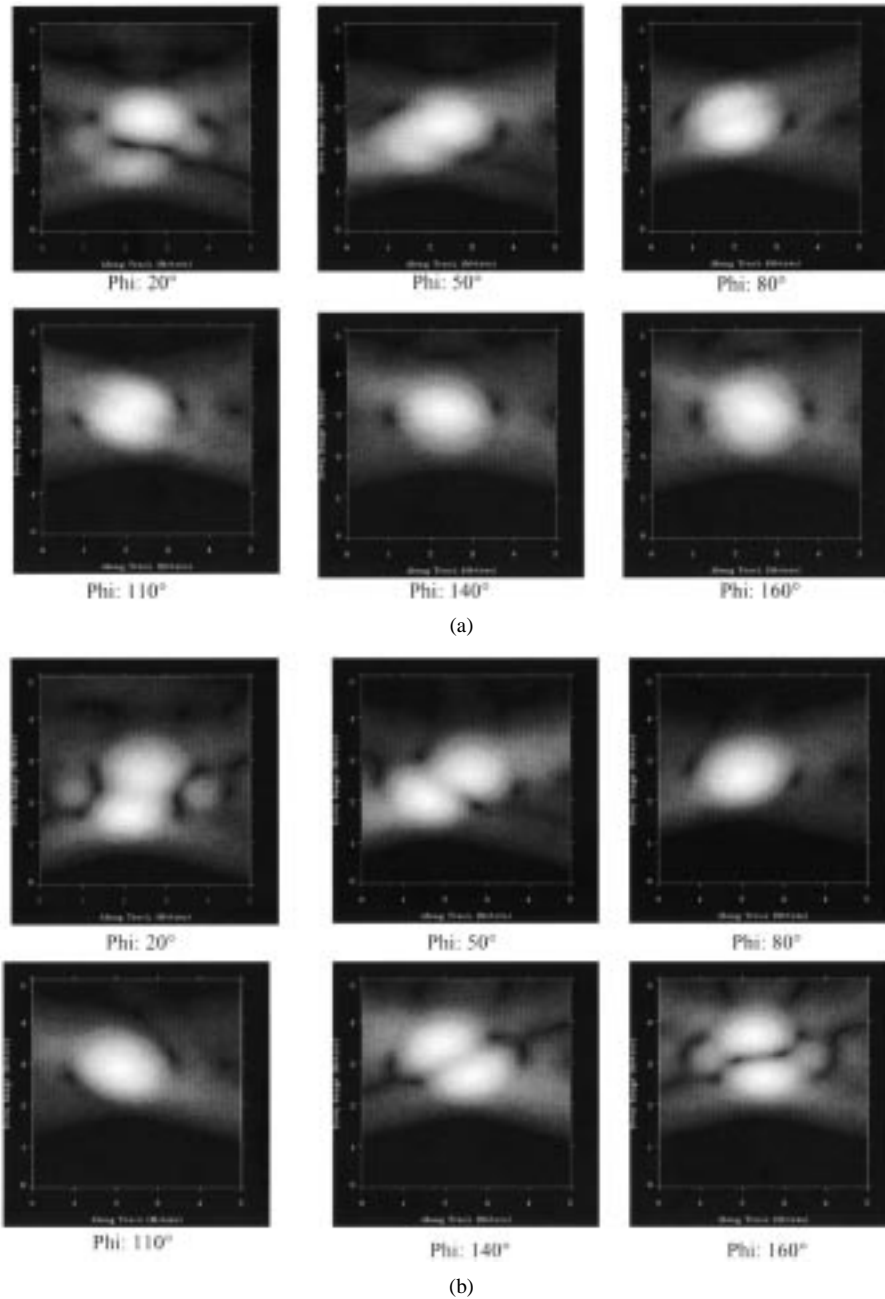


Fig. 9. Synthetic aperture radar (SAR) images of the tree trunk considered in Figs. 7–8. The SAR has the incident waveform in Fig. 2, and the angle between the sensor and tree-trunk axis is fixed at  $50^\circ$ , and a  $35^\circ$  SAR aperture is assumed, relative to the tree axis. Results are shown for apertures centered at the azimuthal positions (see Fig. 1)  $\phi = 20^\circ$ ,  $\phi = 50^\circ$ ,  $\phi = 80^\circ$ ,  $\phi = 110^\circ$ ,  $\phi = 140^\circ$ , and  $\phi = 160^\circ$ . In all images the dynamic range is fixed at 40 dB (white strongest, black weakest). The peak image strength is weakest for azimuthal positions near  $\phi = 0^\circ$  and  $\phi = 180^\circ$ , and strongest near  $\phi = 90^\circ$  (see Fig. 8). (a)  $VV$  polarization and (b)  $HH$  polarization.

ment is expected to be a strong function of the incidence angle. By contrast, this is expected to be a much smaller effect for  $HH$  polarization, for which the penetration is relatively small.

#### D. Tilted Terrain

We next consider the scattered return from a tree trunk over a sloped terrain, with soil electrical parameters characteristic of Yuma soil with 10% water content [20]. A  $10^\circ$  slope is considered, with a tree trunk of 30 cm diameter, 5 m height, permittivity  $\epsilon = \epsilon_0(3 - j0.5 - j\sigma/\omega\epsilon_0)$ , and conductivity  $\sigma = 0.005$  S/m. The tree trunk axis makes an angle  $\theta_T = 80^\circ$  with

respect to the terrain slope (see Fig. 1). The BoR MoM model is inappropriate for this example, and therefore, all associated MoM data have been computed with the triangular-patch model. We consider an incidence angle of  $50^\circ$  relative to the tree-trunk axis for all azimuthal positions considered. This was selected to be consistent with a SAR system flying at a fixed height, and at a constant radius relative to the tree axis. For reference, the azimuthal positions  $\phi = 0^\circ$  and  $\phi = 180^\circ$  are shown in Fig. 1.

In Fig. 7, we consider the RCS for  $HH$  polarization. Since for this incidence angle and terrain slope mechanism i) is not observed in backscatter, the RCS calculations in Fig. 7 include mechanisms ii)-iv). For the case  $\phi = 0^\circ$  and  $\phi = 180^\circ$  in

Fig. 7(a) and (b), respectively, we see the agreement between the MoM and approximate solutions is relatively good. It is interesting to note that in this case, unlike in the previous  $HH$  results (for flat terrain), there are sharp dips in the frequency-dependent RCS response. This is because here, unlike in Figs. 4–6, there is no dihedral response i) in Fig. 1 to dominate the RCS. Hence, the frequency-dependent interference between the other scattering mechanisms dominates the RCS, yielding the characteristics in Fig. 7. We also performed similar comparisons between the MoM and approximate solutions for the  $VV$  polarization, and in that case the agreement between the MoM and approximate solution was considerably worse.

When the tree trunk is normal to the air-ground interface, the scattered fields are independent of the azimuthal angle  $\Phi$ , and the cross-polarized backscattered fields are zero. We now address the  $\Phi$ -dependent signature for the sloped-terrain example considered in Fig. 7. The time-domain backscattered fields for  $\phi = 0^\circ, 45^\circ, 135^\circ$  and  $180^\circ$  are shown in Figs. 8(a)–8(d), respectively. Due to bisectional symmetry, the cross-polarized backscattered fields vanish at  $\phi = 0^\circ$  and  $\phi = 180^\circ$  (see Fig. 1). In all cases the incident plane wave has an angle  $\theta_i = 50^\circ$  relative to the tree axis, with an incident-pulse shape as in Fig. 2. A close inspection of the results in Fig. 8 for  $HH$  and  $VV$  polarizations reveals that, for a given polarization, the initial scattered waveform, representative of mechanism ii) in Fig. 1, is independent of the azimuthal orientation  $\phi$ . Further, theoretically, there should be no cross-polarized component to mechanism ii), since the top of the target is theoretically rotationally symmetric, and mechanism ii) is independent of the ground slope. However, in Fig. 8(b) and (c) we note that there is a small cross polarized diffracted component representative of mechanism ii). This is due to the fact that the triangular-patch discretization yields a target mesh that is not exactly rotationally symmetric [4], [12]. Hence, the small initial diffracted component in Fig. 8(b) and (c) is reflective of this asymmetry.

After the arrival of mechanism ii), there is a stronger scattered waveform, which appears to be the composite of *two* pulses, slightly delayed with respect to each other. This representation of two delayed pulses is particularly clear, for example, in the  $HH$  signature of Fig. 8(b). We attribute these two time-delayed waveforms to mechanisms iii) and iv) in Fig. 1. For some of the examples, there is appreciable scattered energy that comes later in time, this reflective of multiple interactions. It is clear from Fig. 8 that the transient scattered fields from a tree trunk over sloped terrain are a strong function of orientation.

### E. Synthetic Aperture Radar

The results in Fig. 8 indicate that the time-dependent scattered waveform is a strong function of orientation for a tree trunk over a sloped terrain. A synthetic aperture radar (SAR) system implicitly views a target from multiple orientations. To address the impact of the aspect-dependent signatures in Fig. 8 on a subsequent SAR image, we consider a SAR system that is flying in a circular path around the tree trunk considered in Fig. 8 (with the same 10% Yuma soil [20]). The SAR is positioned such that a constant angle of incidence exists between the sensor and the tree axis and, as in Fig. 7, this is assumed to be  $\theta_i = 50^\circ$ . The SAR is assumed to span a  $35^\circ$  aperture with respect to the target center, and here each aperture position is weighted equally i.e., the antenna pat-

tern is assumed uniform over approximately  $35^\circ$ ). Simple back-projection of the time domain fields (as in Fig. 8) is used to form the SAR image. In Fig. 9, we present SAR images using data computed via the triangular-patch MoM model, for six different center positions of the  $35^\circ$  aperture. In particular, we consider apertures centered at  $20^\circ, 50^\circ, 80^\circ, 110^\circ, 140^\circ$ , and  $160^\circ$ , where Fig. 9(a) and 9(b) are for  $VV$  and  $HH$  polarization, respectively. As expected from Fig. 8, the SAR image is a strong function of the aperture position. At particular positions [e.g.,  $\phi = 160^\circ$  in Fig. 9(b)], the image is characterized by two strong regions, these likely due to separated responses from mechanisms iii) and iv), while for other sensor positions, these two returns coalesce into a single strong return.

## IV. CONCLUSIONS

Three models have been presented for electromagnetic scattering from a tree trunk over a half space. Two of the models were based on the MoM, with one MoM model restricted to the special case of a body of revolution (BoR) and the other employing a general triangular-patch basis function decomposition. In addition, we considered an approximate model based on the series-expansion solution for scattering from an infinite dielectric cylinder. For the VHF frequencies considered, we found that the approximate solution was in excellent agreement with the numerical solutions for  $HH$  polarization, with this agreement degrading slightly for  $VV$  polarization (for the sloped-terrain case, the approximate solution was particularly poor for  $VV$  polarization). The numerical models were employed to investigate the backscattered signature from a tree trunk in both the frequency and time domain. Results were presented as a function of tree-trunk height, diameter, and electrical parameters. Moreover, we considered the backscattered RCS for various incident angles. We also considered backscattering from a tree trunk on sloped terrain, both in the time domain and in the SAR image domain. These examples have demonstrate that, despite the relative simplicity of the tree-trunk target, the associated scattering phenomenology is quite complicated and must be considered carefully in the context of foliage penetrating (FOPEN) radar.

Despite the fact that, to our knowledge, this paper represents the most rigorous analysis of tree-trunk scattering to date, there are still many issues that need to be addressed further. In particular, we demonstrated in Fig. 1 that there are four principal scattering mechanisms of interest for tree-trunk scattering. Two of these, ii) and iii) in Fig. 1, are driven by diffraction from the top of the tree trunk. Unfortunately, this is the least realistic aspect of the scattering model. Dihedral scattering between the tree-trunk surface and the soil interface is accounted for accurately, but this phenomenon is not generally present for the case of sloped terrain. For such circumstances, the scattered fields computed by the simple model in Fig. 1 are driven in large part by diffraction at the “top” of the tree trunk, this being a simple approximation for the scattering mechanisms of an actual tree. Thus, for the flat-terrain case the principal (dihedral) scattering mechanism is well represented, but for the tilted-terrain case there are significantly more approximations. Consequently, the scattering physics predicted by the model must be validated by measurements. Moreover, the triangular-patch model is appli-

cable to general dielectric targets in the presence of a layered medium (soil). Future work will involve the use of this model to more realistically handle the large branches in the tree, these potentially being important at the VHF and low-UHF frequencies of interest. We have emphasized throughout, however, that the computational burden of such electrically large problems is prohibitive for the MoM solver. The limitations in the MoM have been ameliorated of late through development of the fast multipole method (FMM) and the multilevel fast multipole algorithm (MLFMA) [23]–[25]. These methods have been used primarily for free-space scattering [17], [18] and for perfectly conducting targets over a half space [25]. For the targets of interest here, the FMM/MLFMA must be extended to general dielectric targets over a half space.

We close by acknowledging that, despite the large number of examples presented here, such a presentation can never be entirely complete within the constraints of brevity. We note, therefore, that in addition to being applicable to constant-radius tree trunks, like those considered here, the BoR and triangular-patch MoM models are also applicable to more general tree-trunk shapes. Orientation-independent curvature in the tree-trunk shape can be handled via the BoR model, while the triangular-patch model is applicable to even more general tree trunk shapes (e.g., elliptical cross section). We found in the course of this work, for example, that small changes in the height-dependent tree radius (appropriate for the BoR model) produce relatively modest changes in the backscatter RCS. A further investigation of such higher-order effects may also be warranted, the focus here being on the principal scattering mechanisms.

#### REFERENCES

- [1] D. R. Sheen, N. P. Malinas, D. W. Kletzli, T. B. Lewis, and J. F. Roman, "Foliage transmission measurements using a ground-based ultra-wideband (300–1300 MHz) SAR system," *IEEE Trans. Geosci. Remote Sensing*, vol. 32, pp. 118–130, Jan. 1994.
- [2] S. G. Leblanc, P. Bicheron, J. M. Chen, M. Leroy, and J. Cihlar, "Investigation of directional reflectance in boreal forests with an improved four-scale model and airborne POLDER data," *IEEE Trans. Geosci. Remote Sensing*, vol. 37, pp. 1396–1414, May 1999.
- [3] N. Geng and L. Carin, "Wide-band electromagnetic scattering from a dielectric BOR buried in a layered lossy dispersive medium," *IEEE Trans. Antennas Propagat.*, vol. 47, pp. 610–619, Apr. 1999.
- [4] S. M. Rao, D. R. Wilton, and A. W. Glisson, "Electromagnetic scattering by surfaces of arbitrary shape," *IEEE Trans. Antennas Propagat.*, vol. 30, pp. 409–418, May 1982.
- [5] Y. C. Lin and K. Sarabandi, "Electromagnetic scattering model for a tree trunk above a tilted ground plane," *IEEE Trans. Geosci. Remote Sensing*, vol. 33, pp. 1063–1070, July 1995.
- [6] L. Tsang, K. H. Ding, G. Zhang, C. Hsu, and J. A. Kong, "Backscattering enhancement and clustering effects of randomly distributed dielectric cylinders overlying a dielectric half space based on Monte-Carlo simulations," *IEEE Trans. Antennas Propagat.*, vol. 43, pp. 488–499, May 1995.
- [7] L. Tsang, C. H. Chan, J. A. Kong, and J. Joseph, "Polarimetric signatures of a canopy of dielectric cylinders based on first and second order vector radiative transfer theory," *J. Electromagn. Waves Appl.*, vol. 6, pp. 19–51, 1992.
- [8] K. Sarabandi, P. F. Polatin, and F. T. Ulaby, "Monte carlo simulation of scattering from a layer of vertical cylinders," *IEEE Trans. Antennas Propagat.*, vol. 41, pp. 465–475, 1993.
- [9] G. Zhang, L. Tsang, and Z. Chen, "Collective scattering effects of trees generated by stochastic Lindenmayer systems," *Microwave Opt. Tech. Lett.*, vol. 11, pp. 107–111, Feb. 1996.
- [10] S. H. Yueh, J. A. Kong, J. K. Jao, R. T. Shin, Shin, and T. LeToan, "Branching model for vegetation," *IEEE Trans. Geosci. Remote Sensing*, vol. 30, pp. 390–402, 1992.

- [11] Z. Chen, "Microwave remote sensing of vegetation: stochastic Lindenmayer systems, collective scattering effects, and neural network inversions," Ph.D. dissertation, Dept. Elect. Eng., Univ. Washington, Seattle, 1994.
- [12] J. He, T. Yu, N. Geng, and L. Carin, "Method-of-moments analysis of electromagnetic scattering from a general three-dimensional dielectric target embedded in a multi-layered medium," *Radio Sci.*, Feb. 2000.
- [13] A. W. Glisson, "Integral equation techniques," in *Dielectric Resonators*, D. Kaifez, Ed. Dedham, MA: Artech House, 1986, pp. 259–325.
- [14] K. A. Michalski and D. Zheng, "Electromagnetic scattering and radiation by surfaces of arbitrary shape in layered media, parts I and II," *IEEE Trans. Antennas Propagat.*, vol. 38, pp. 335–352, Mar. 1990.
- [15] Y. Rahmat-Samii, R. Mittra, and P. Parhami, "Evaluation of sommerfeld integrals for lossy half-space problems," *Electromagnetics*, vol. 1, no. 1, pp. 1–28, 1981.
- [16] R. M. Shubair and Y. L. Chow, "A simple and accurate complex image interpretation of vertical antennas present in contiguous dielectric half-spaces," *IEEE Trans. Antennas Propagat.*, vol. 41, pp. 806–812, June 1993.
- [17] Y. L. Chow, J. J. Yang, D. G. Fang, and G. E. Howard, "A closed-form spatial Green's function for the thick microstrip substrate," *IEEE Trans. Microwave Theory Tech.*, vol. 39, pp. 588–562, Mar. 1991.
- [18] M. L. V. Blaricum and R. Mittra, "A technique for extracting the poles and residues of a system directly from its transient response," *IEEE Trans. Antennas Propagat.*, vol. 23, pp. 777–781, Nov. 1975.
- [19] Y. Hua and T. K. Sarkar, "Matrix pencil method for estimating parameters of exponentially damped/undamped sinusoids in noise," *IEEE Trans. Acousti., Speech, Signal Process.*, vol. 38, pp. 814–824, May 1990.
- [20] L. Carin, N. Geng, M. McClure, J. Sichina, and L. Nguyen, "Ultra-wide-band synthetic-aperture radar for mine-field detection," *IEEE Antennas Propagat. Mag.*, vol. 41, pp. 18–33, Feb. 1999.
- [21] L. Carin, R. Kapoor, and C. E. Baum, "Polarimetric SAR imaging of buried landmines," *IEEE Trans. Geosci. Remote Sensing*, vol. 36, pp. 1985–1988, Nov. 1998.
- [22] J. E. Hipp, "Soil electromagnetic parameters as functions of frequency, soil density, and soil moisture," *Proc. IEEE*, vol. 62, pp. 98–103, Jan. 1974.
- [23] J. M. Song and W. C. Chew, "Multilevel fast multipole algorithm for solving combined field integral equations of electromagnetic scattering," *Microwave Opt. Tech. Lett.*, vol. 10, pp. 14–19, Sept. 1995.
- [24] X. Q. Sheng, J. M. Jin, J. Song, W. C. Chew, and C. C. Lu, "Solution of combined-field integral equations using multilevel fast multipole algorithm for scattering by homogeneous bodies," *IEEE Trans. Antennas Propagat.*, vol. 46, pp. 1718–1726, Nov. 1998.
- [25] N. Geng, A. Sullivan, and L. Carin, "Multi-level fast-multipole algorithm for scattering from conducting targets above or embedded in a lossy half space," *IEEE Trans. Geosci. Remote Sensing*, to be published.

**Jiangqi He** was born in China. He received the M.S.E.E. degree from New Mexico State University, Las Cruces, in 1998 and the Ph.D. degree in electrical engineering from Duke University, Durham, NC, in 2001.

He joined Intel Corporation, Phoenix, AZ, in 2001, where he is developing techniques for the analysis of high-frequency integrated circuits. His research interests include numerical methods for wideband electromagnetic scattering and propagation as well as high-speed integrated circuits.

**Norbert Geng** (S'91–M'96) was born May 14, 1965 in Lauchringen, Germany. He received the Dipl.-Ing. and Dr.-Ing. degrees in electrical engineering from the University of Karlsruhe, Germany, in 1991 and 1996, respectively.

From 1991 to 1996, he was with the Institute for Microwaves and Electronics, University of Karlsruhe, Karlsruhe, Germany, working on full-wave propagation modeling for radio communications systems. In January 1997, he joined the Department of Electrical and Computer Engineering, Duke University, Durham, NC, as a visiting Postdoctoral Researcher for 18 months. While visiting Duke University, and for another 18 months at the University of Karlsruhe, his research focused on numerical techniques in computational electromagnetics for planar-stratified media. In January 2000, he joined SIEMENS Corporate Technology, Munich, Germany, working as a Research Scientist on the design of broadband wireless communications systems.

Dr. Geng received the Mannesmann Innovation Award in 1997 for his dissertation on full-wave propagation modeling for radio communications systems.

**Lam Nguyen** was born on January 16, 1961, in Vietnam. He received the B.S.E.E. degree from Virginia Polytechnic Institute, Blacksburg, the M.S.E.E. degree from George Washington University, Washington, DC, and the M.S.C.S. degree from Johns Hopkins University, Baltimore, MD, respectively.

He was with General Electric from 1984 to 1985. He has been with the Army Research Laboratory and its predecessor organization, Harry Diamond Laboratory since 1986. He has been primarily engaged in the research and development of foliage penetratuib and pround penetration via ultrawideband (UWB) radars. His primary research interests include digital signal processing and algorithm development.

**Lawrence Carin** (SM'96–F'01) was born March 25, 1963 in Washington, DC. He received the B.S., M.S., and Ph.D. degrees in electrical engineering from the University of Maryland, College Park, in 1985, 1986, and 1989, respectively.

In 1989, he joined the Electrical Engineering Department, Polytechnic University, Brooklyn, NY, as an Assistant Professor, and became an Associate Professor there in 1994. In September 1995, he joined the Electrical Engineering Department at Duke University, Durham, NC, where he is now a Professor. He is the Principal Investigator on a Multidisciplinary University Research Initiative (MURI) on demining. His current research interests include short-pulse scattering, subsurface sensing, and wave-based signal processing.

Dr. Carin is a member of the Tau Beta Pi and Eta Kappa Nu honor societies and is currently an Associate Editor of the IEEE TRANSACTIONS ON ANTENNAS AND PROPAGATION.